



Flower-like MoS₂ on graphitic carbon nitride for enhanced photocatalytic and electrochemical hydrogen evolutions

Yazi Liu^a, Xinyuan Xu^b, Jinqiang Zhang^b, Huayang Zhang^a, Wenjie Tian^a, Xiaojie Li^a, Moses O. Tade^a, Hongqi Sun^{b,*}, Shaobin Wang^{a,*}

^a Department of Chemical Engineering, Curtin University, GPO Box U1987, Perth, WA 6845, Australia

^b School of Engineering, Edith Cowan University, Joondalup, WA 6027, Australia



ARTICLE INFO

Keywords:

MoS₂
Photocatalysis
Electrochemical reduction
Hydrogen evolution reaction (HER)
g-C₃N₄

ABSTRACT

Design of highly efficient catalysts has already been a challenge in the exploration of renewable energies based on nanotechnologies. Herein, a feasible strategy of three-dimensional (3D)/two-dimensional (2D) nanojunctions was employed to achieve a prominently enhanced activity in both solar hydrogen evolution and electrochemical hydrogen generation from water splitting. Flower-like MoS₂ nanoparticles with thin-layers were fabricated using a one-pot hydrothermal process and were further attached to g-C₃N₄ nanosheets via their (002) crystal planes to form an intimate face-to-face contact. The hybrid catalysts exhibited a red-shift to the visible light region with an enhanced absorption capacity. At the optimal loading of 0.5 wt% MoS₂, MoS₂/g-C₃N₄ exhibited the highest photocatalytic H₂ evolution rate of 867.6 μmol h⁻¹ g⁻¹ under simulated sunlight irradiations, which is 2.8 times as high as that of pure g-C₃N₄. Furthermore, the average photocatalytic H₂ evolution rate was elevated to ca. 5 times as high as that of pure g-C₃N₄ under visible light irradiations. The synergistic effect responsible for the enhanced HER (hydrogen evolution reaction) performance might be originated from the intimate interface between the light-harvesting g-C₃N₄ and MoS₂ as the active sites with the decreased overpotential, lowered charge-transfer resistance and increased electrical conductivity, leading to a more efficient charge separation and a higher reductive potential. In addition, the lower overpotential and smaller Tafel slope on 0.5 wt% MoS₂/g-C₃N₄ lead to the enhancement of electrochemical HER performance compared to pure g-C₃N₄. This work provides a feasible protocol for rational design of highly efficient HER electrocatalysts and photocatalysts towards future energy innovation.

1. Introduction

As a clean and renewable energy carrier, hydrogen has been extensively acknowledged as an ideal source to mitigate the severe global energy crisis and environmental deterioration [1,2]. Photocatalytic H₂ evolution utilizing solar energy as well as electrochemical H₂ evolution reaction (HER) via water splitting has aroused significant research interests worldwide [3–7]. Since Fujishima and Honda for the first time developed a TiO₂-based photoelectrochemical water splitting cell in 1972 [8], numerous catalytic systems composed of an earth-abundant light-harvesting photocatalyst with an electronic conductive co-catalyst, especially noble-metal, have been constructed to achieve highly efficient photocatalytic H₂ evolution [9–12].

Most recently, two-dimensional (2D) semiconductors with a unique structure have triggered broad interests owing to their unprecedented optical and electronic properties [13,14]. Among them, graphitic

carbon nitride (g-C₃N₄) has attracted overwhelming research focus because of its narrow band gap, strong photoreduction capability as well as easy production from nitrogen-rich precursors [15–17]. Despite these fascinating merits, pure g-C₃N₄ still suffers from several shortfalls such as limited light absorption, easy recombination of electron/hole pairs and sluggish electrical conductivity. To resolve these bottlenecks, a strategy of incorporating 2D g-C₃N₄ with another co-catalysts with lamellar structures to form hybrid nanocomposites with an intimate contact interface has been proven to be highly effective with practical capabilities [18,19]. Meanwhile, an ideal co-catalyst might also serve as the active sites to decrease the overpotentials for electrocatalytic H₂ evolution and lower the charge-transfer resistance to enhance the HER performance of g-C₃N₄ [20]. Among a variety of layered materials, molybdenum sulfide (MoS₂) has demonstrated its excellent HER performance and can act as an efficient co-catalyst for solar-to-H₂ conversion [21,22–23]. The similarity of the layered structures between

* Corresponding authors.

E-mail addresses: h.sun@ecu.edu.au (H. Sun), Shaobin.wang@curtin.edu.au, shaobin.wang@exchange.curtin.edu.au (S. Wang).

MoS_2 and $\text{g-C}_3\text{N}_4$ poses positive effects on charge transfer and formation of a newly built electric field at the interface between MoS_2 and $\text{g-C}_3\text{N}_4$ modulates the electronic band structures. Moreover, the unsaturated Mo and S atoms at the exposed edges will also promote the sulfur edge activity functioning as active sites [24]. So far, most of the reported $\text{MoS}_2/\text{g-C}_3\text{N}_4$ hybrids were constructed as either 2D (MoS_2)/2D ($\text{g-C}_3\text{N}_4$) or 0D (MoS_2)/2D ($\text{g-C}_3\text{N}_4$) heterojunctions via a complicated impregnation-sulfidation approach or under harsh reaction conditions [14,25–27]. However, 2D MoS_2 layers tend to restack or aggregate due to van der Waals interaction. It is suggested that a three-dimensional flower-like MoS_2 consisting of few-layer nanosheets may suppress the sheets stacking to expose more active edge planes [24], exhibiting a larger surface area with shorter transport paths, higher interfacial transfer, and much enhanced photoactivity [28,29]. Thus, a simple and green technology for the fabrication of such hybrid nanocomposites with greatly enhanced electrocatalytic and photocatalytic activities is needed to be demonstrated.

Herein, a functional hybrid of 3D (MoS_2)/2D ($\text{g-C}_3\text{N}_4$) nanojunction with an intimate face contact was fabricated via a feasible and sustainable ultrasonic approach. In which, a unique flower-like MoS_2 superstructure with self-assembled ultrathin nanosheets with exposed (103) and (002) facets was synthesized using a facile, one-pot hydrothermal process, assisted by N-acetyl-l-cysteine as a biomolecular capping reagent to control the morphology and growth of MoS_2 nanosheets for the first time. The as-prepared hybrids exhibited drastically enhanced photocatalytic and electrocatalytic H_2 -evolution activities, compared to pure $\text{g-C}_3\text{N}_4$, 2D (MoS_2)/2D ($\text{g-C}_3\text{N}_4$) and 0D (MoS_2)/2D ($\text{g-C}_3\text{N}_4$). The optimal 0.5% 3D (MoS_2)/2D ($\text{g-C}_3\text{N}_4$) hybrid demonstrated superior photocatalytic activity and stability for H_2 evolution under solar and visible lights. Moreover, the 0.5% 3D (MoS_2)/2D ($\text{g-C}_3\text{N}_4$) also showed an excellent electrocatalytic HER activity with a low overpotential and substantial current densities. Finally, the in-depth probe on photocatalytic mechanism reveals that the intimate contact interface contributes to a higher photoreductive potential, a faster interfacial charge separation and electrons transfer from $\text{g-C}_3\text{N}_4$ to MoS_2 to facilitate the overall photocatalytic H_2 evolution reaction.

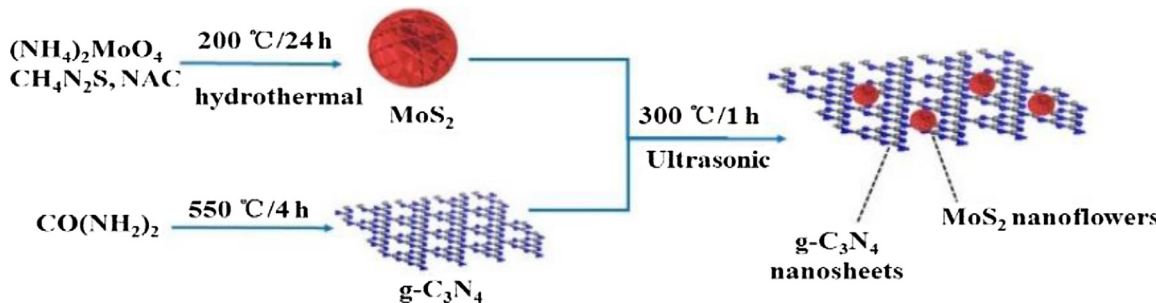
2. Experimental

2.1. Materials

Urea ($\geq 99.5\%$, pellets), ammonium molybdate (99.98%), N-acetyl-l-cysteine(NAC, $\geq 99\%$), thiourea ($\geq 99.0\%$), chloroplatinic acid hexahydrate ($\geq 37.5\%$ Pt basis), anhydrous ethanol, and methanol were supplied by Sigma-Aldrich, Australia. All the reagents were directly used as received.

2.2. Synthesis of the catalysts

The 3D (MoS_2)/2D ($\text{g-C}_3\text{N}_4$) binary photocatalysts with the unique structure were successfully fabricated via a facile and reliable ultrasonic approach as illustrated in Scheme 1.



Scheme 1. Synthesis process of 3D (MoS_2)/2D ($\text{g-C}_3\text{N}_4$) nanocomposites.

Metal-free $\text{g-C}_3\text{N}_4$ (CN) powders were synthesized using urea as the precursor. Typically, 10 g of urea was placed in a furnace with a cover, heated to 550 °C at a rate of 5 °C min⁻¹ and kept at 550 °C for 4 h in air.

MoS_2 nanostructured (MSNS) particles were synthesized based on a facile one-pot hydrothermal approach[30] with prolonged reaction time. Ammonium molybdate (33.32 mg) and N-acetyl-l-cysteine (66.58 mg) were dissolved in 40 mL ultrapure water in an ice-water bath. Thiourea (25.88 mg) was added to the above solution with further stirring for 1 h under N_2 protection. The mixture was subsequently transferred into a 100-mL Teflon-lined stainless steel autoclave which was already de-aired with N_2 flow, and kept at 200 °C for 24 h to form black sediments of MoS_2 . Afterwards, the black precipitates were filtered and washed with ethanol and deionized (DI) water, followed by drying overnight at 80 °C.

Binary MSNS-CN composites were synthesized by an ultrasonic chemical approach. The as-synthesized $\text{g-C}_3\text{N}_4$ powder (0.1 g) and a certain amount of MoS_2 were dispersed in 10 mL anhydrous ethanol with ultrasonic shaking for 1 h, followed by vigorous stirring for 10 h before being dried at 80 °C to remove the solvent. At last, the samples were further heated under N_2 flow at 300 °C for 1 h to strengthen the interaction between the MoS_2 nanostructure and $\text{g-C}_3\text{N}_4$ matrix. The weight ratios of MoS_2 to $\text{g-C}_3\text{N}_4$ were varied from 0 to 2.5% and noted as x% MSNS-CN, where x = 0, 0.1, 0.2, 0.5, and 2.5 representing different weight ratios of MoS_2 at 0, 0.1 wt%, 0.2 wt%, 0.5 wt%, and 2.5 wt%, respectively.

2.3. Characterization techniques

Thermogravimetric analysis (TGA) was performed on a TGA 4000 analyzer (Perkin Elmer) with a heating rate of 10 °C min⁻¹. X-ray diffraction (XRD) patterns were obtained on Panalytical Empyrean multipurpose research diffractometer utilizing a Cu K α radiation ($\lambda = 1.5418 \text{ \AA}$). Transition electron microscopy (TEM) and high-resolution transmission electron microscopy images were collected on a JEOL 2100 TEM microscope. The high angle annular dark field scanning transmission electron microscopy (HAADF-STEM) images were recorded with FEI TITAN G2 (200 kV). Fourier transform infrared (FTIR) spectra were recorded on a PerkinElmer Spectrum 100 spectrometer in the range of 500–2000 cm⁻¹. X-ray photoelectron spectroscopy (XPS) measurements were conducted on a Thermo Escalab 250 with an Al K α X-ray. A Shirley background was first subtracted followed by component fitting using Voigt functions with a 30% Lorentzian component. Raman spectra were obtained on a confocal microscopic Raman spectrometer (WITec alpha 300RA+) using a 785 nm laser as irradiation light. UV-vis diffuse reflectance spectra (DRS) were recorded on an Agilent Cary 100 UV-vis spectrophotometer equipped with an integrated sphere attachment. Photoluminescence (PL) spectra of the samples were obtained on an Agilent Cary Eclipse Fluorescence Spectrophotometer.

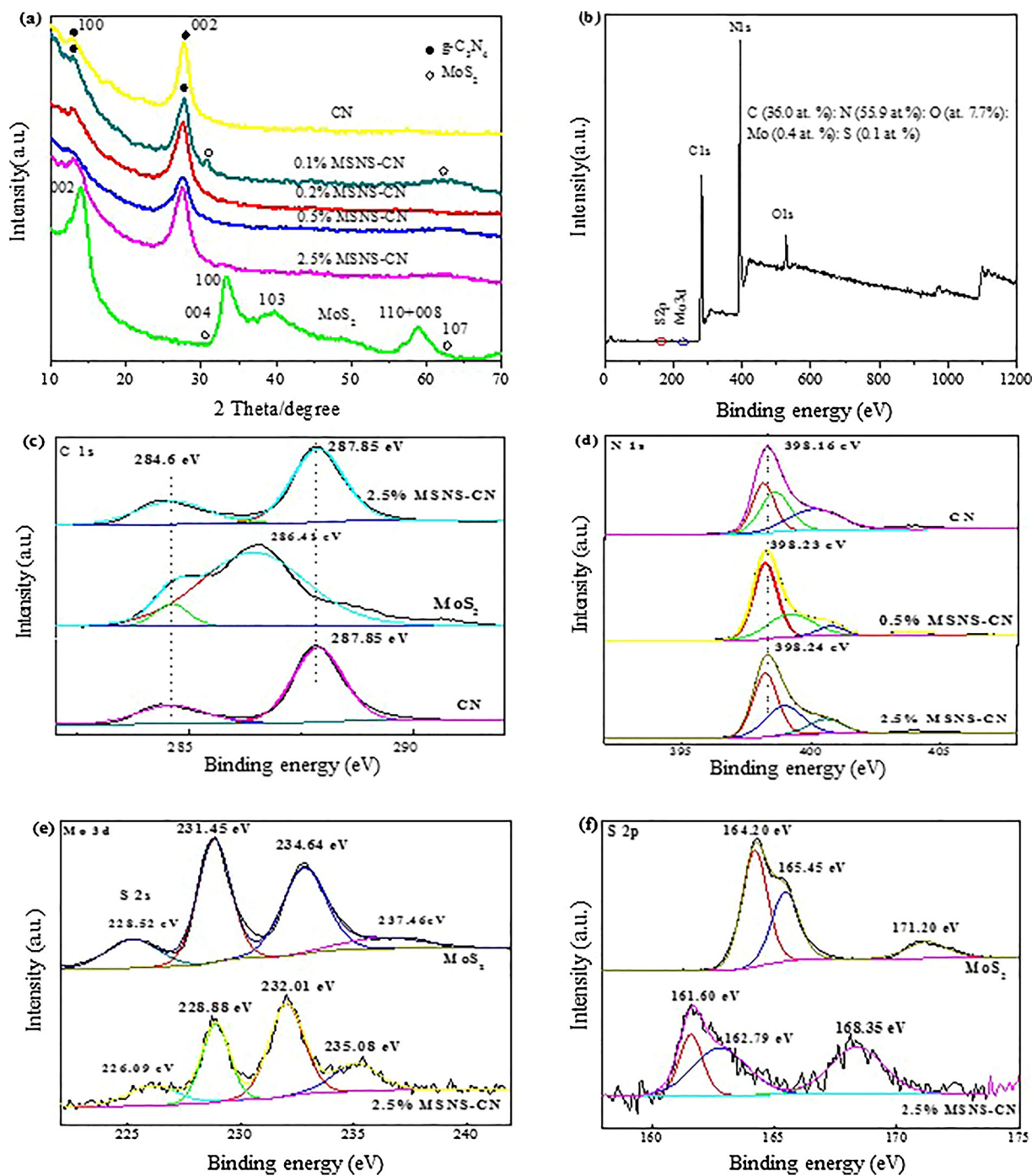


Fig. 1. (a) XRD patterns of pure g-C₃N₄ and MSNS-CN composite samples; (b) XPS survey of 0.5% MSNS-CN; High-resolution XPS spectra of (c) C 1s (d) N 1s (e) Mo 3d and (f) S 2p of some samples.

2.4. Evaluation of photocatalytic activity

The photocatalytic hydrogen evolution experiments were conducted in a stainless steel vessel sealed with a quartz window for top-irradiation. A 300 W Xeon lamp (Newport) was used as the simulated solar light source with an irradiation intensity at 35 mW cm⁻² for UV light and 300 mW cm⁻² for visible light using a light cutoff filter ($\lambda > 420$ nm). The hydrogen evolution reaction was performed by dispensing 50 mg of photocatalyst powder in 120 mL of aqueous solution containing 25% methanol by volume. The loading of 2.0 wt% Pt co-catalyst was conducted by directly dissolving H₂PtCl₆ into the suspension, followed by ultrasonication for 30 min. Prior to irradiation, the

suspensions were mixed under vigorous stirring for 30 min in dark and the reaction vessel was evacuated to remove air completely by purging with N₂. The produced H₂ was in situ analyzed by a gas chromatography (Agilent 490 Micro GC) using a thermal conductivity detector.

2.5. Photoelectrochemical measurements

Photocurrent, electrochemical impedance spectroscopy (EIS) and Mott-Schottky curve measurements were performed on a Zahner Zennium electrochemical workstation in a standard three-electrode framework with a 0.05 M Na₂SO₄ (pH = 6.8) electrolyte solution, adopting a Pt wire as the counter electrode and a saturated calomel

electrode (SCE) as the reference electrode. As for the photoanode, the sample film was fabricated on a fluorine-doped tin oxide (FTO) glass, which was ultrasonically cleaned in acetone and ethanol for 20 min in sequence, then dried at 60 °C. To be specific, 10 mg of the catalyst was mixed with 500 µL of absolute ethanol and 25 µL of Nafion solution homogeneously. The obtained slurry was then dropped onto the pre-treated FTO glass via a dip-coating method with a controlled area of 1 cm², followed by drying in air for 2 h to form a film electrode. Photocurrents were obtained using a 300 W Xenon arc lamp with light passing through an AM 1.5 G filter into an optical fiber (output $I_0 = 100 \text{ mW} \cdot \text{cm}^{-2}$).

2.6. Electrocatalytic hydrogen evolution

Electrochemical measurements were carried out at room temperature on a Zennium electrochemical station (Zahner, Germany) in a standard three-electrode system, using the samples on the glassy carbon electrode (GCE, 5 mm in diameter) as the working electrode, an Ag/AgCl electrode as the reference and a Pt wire as the counter electrode. The electrolyte was 0.5 M H₂SO₄ purged with N₂ gas (99.999%). The catalysts of 5 mg were dispersed in 600 µL absolute ethanol and 50 µL 5% Nafion via ultrasonication for 1 h to form a homogeneous ink. Then 5 µL of the slurry was deposited on a glassy carbon electrode with a catalyst loading of 0.196 mg cm⁻². The HER performance was tested by linear sweep voltammetry (LSV) at a scan rate of 10 mV S⁻¹.

3. Results and discussion

3.1. Crystal structure, morphology and composition

Thermogravimetric analysis (TGA) was implemented to determine the actual mass ratios of MSNS-CN samples. All of the TGA curves in Fig. S1 show similar profiles. Compared to pure g-C₃N₄, the TGA curves of all MSNS-CN samples exhibit significant decay at lower temperature for both starts and ends, suggesting that the obtained MSNS-CN samples possess lower thermal stability, probably due to the crystallization disturbance from MoS₂ [31]. The weight loss under 400 °C could be ascribed to the oxidation process from MoS₂ to MoO₃ [31,32]. The rapid decay above 450 °C represents the thermal decomposition of g-C₃N₄. Assuming that the final product after 550 °C is pure MoO₃, MoS₂ contents were calculated to be 0.12%, 0.18%, 0.36% and 0.92%, corresponding to 0.1%, 0.2%, 0.5% and 2.5% MSNS-CN as-synthesized samples, respectively.

XRD was used to investigate the crystal structures of pure MoS₂ and hybrid MSNS-CN samples at varying MoS₂ contents of 0–2.5 wt% (Fig. 1a). All the MSNS-CN samples follow the similar pattern of pure g-C₃N₄ with two distinct diffraction peaks at 27.6° and 13.1°, representing the interplanar stacking of the conjugated double bonds for graphitic materials as the (002) crystal plane and the in-planar ordering of tri-s-triazine units as the (100) plane [33], respectively. As for pure MoS₂, all the diffraction peaks conform to the typical pattern of hexagonal 2H-MoS₂ structure (JCPDS No. 37-1492) [21] with apparent broadening and shortening of all the peaks, suggesting a smaller average crystallite size and less layers of MoS₂ nanosheets with a well-stacked lamellar structure, compared to bulk MoS₂ [34–36]. The MSNS-CN composite samples exhibit strong diffraction peaks of g-C₃N₄, and some tiny peaks of MoS₂ due to the low contents, confirming the existence of both phases. It can be seen that the modification with MoS₂ does not pose any noticeable impact on the bulk structure and chemical skeleton of g-C₃N₄ nanosheet.

The chemical state and surface elemental composition of the 0.5% MSNS-CN sample were examined by XPS (Fig. 1b–e). Fig. 1b gives the XPS full survey spectrum, indicating the existence of elements of C, N, O with a small amount of Mo and S. The corresponding peaks could be observed at binding energies of 287.5 (C 1s), 397.5 (N 1s), 531.5 (O 1s), 231.0 (Mo 3d) and 170.5 eV (S 2p), respectively. An atomic C/N

proportion of 0.64 was detected in the sample, consistent with the theoretical value of pure g-C₃N₄ at 0.75 [37]. Oxygen at 7.7 at.% was also present, which can be ascribed to the prolonged annealing of g-C₃N₄ in the air as well as the adsorbed water molecules [38]. To achieve stronger signal-noise ratio for more convincing evidence, peaks from 2.5% MSNS-CN were also studied in detail after deconvolution, apart from the sample of 0.5% MSNS-CN. For pure g-C₃N₄, C 1s peak in Fig. 1c can be deconvoluted into two peaks at binding energies of ~284.6 and ~287.8 eV, respectively. The former can be assigned to unavoidably loaded graphitic or amorphous carbon atoms adsorbed on the surface (C—C/C=C bonding) [39,40], and the latter is associated with sp²-hybridized carbon in the triazine rings of carbon nitride lattice (N—C=N bonding) [41–44]. As observed, the existence of C elements on the surface of MoS₂ could be ascribed to some graphitic carbon residual from the precursors during the synthesis process, which might explain that the peak intensity of 284.6 eV increased compared to pure g-C₃N₄. Depicted in Fig. 1d, three prominent peaks at 398.16, 398.60, and 400.14 eV can be obtained for pure g-C₃N₄ by deconvoluting N 1s (Fig. 1d), corresponding to sp²-bonded N atoms of C—N=C, tertiary (N—(C)3) groups and amino functional groups (C—N—H) [10,33,45,46]. This further confirms the existence of graphite-like g-C₃N₄ structure. After modification, all the N 1s peaks shift to a higher binding energy with increasing contents of MoS₂. Looking into Fig. 1e, peaks of Mo 3d and S 2s are observed at binding energies of 231.5 (Mo 3d_{5/2}), 234.6 eV (Mo 3d_{3/2}) and 228.5 eV (S 2s) for pure MoS₂, which are the typical values of Mo⁴⁺ peak in MoS₂, convincing the predominant existence of Mo⁴⁺ state. Fig. 1f shows that two strong peaks in S 2p spectrum appear at 164.2 and 165.5 eV, which are assigned to S 2p_{3/2} and S 2p_{1/2}, respectively, indicating the presence of S²⁻ in MoS₂ [47]. Two weak bands at 237.5 eV (Fig. 1e) and 171.2 eV (Fig. 1f) suggest the possible presence of Mo⁶⁺ and S⁶⁺, respectively, owing to the small amount of oxide species during the calcination process. Compared with pure MoS₂, both of Mo 3d and S 2p peaks of 2.5% MSNS-CN shift to a lower binding energy, indicating the change of chemical microenvironment of Mo and S atoms after g-C₃N₄ hybridizes with MoS₂. The opposite shifting tendency between N 1s and Mo 3d (S 2p) suggests that the total electron density has migrated from g-C₃N₄ to MoS₂ due to the stronger electronegativity of S atoms, thus facilitating the change of bonding and the formation of interface. The high-resolution spectra of XPS further confirmed the existence of MoS₂ in the hybridized samples.

The morphology and microstructure of the as-synthesized samples of MoS₂, g-C₃N₄ and 0.5% MSNS-CN were investigated by SEM. As shown in Fig. 2a and b, pure MoS₂ particles demonstrate a 3D flower-like nanostructure with diameters about 400–600 nm and are consisted of thin nanosheets showing thickness around 10 nm. Interestingly, the tiny plate-like subunits interconnected with each other by sharing one edge to form the three-dimensional flower-like networks. The rippled nanoplates in ultrathin features self-assembled to constitute the loose porous architecture to avoid a disordered stacking of MoS₂ layers, which might be beneficial in exposing more edges as active sites and enlarging specific surface area to shorten the diffusion path for both reactant molecules and surface charges [28]. Different from the sheet-like structure of pure g-C₃N₄ in Fig. 2d, the MoS₂/g-C₃N₄ (0.5 wt%) composite in Fig. 2c exhibits more loose and fluffy microstructure, indicating the incorporation and coating of MoS₂ nanoflowers into the matrix of g-C₃N₄ nanosheets. The intimate contact of the 3D MoS₂ superstructure with 2D g-C₃N₄ nanosheets might facilitate the enhancement of photoactivity with the controllable porous nanostructure.

TEM and magnified HRTEM images of g-C₃N₄, MoS₂ and 0.5% MSNS-CN are shown in Fig. S2 and Fig. 3. Derived directly from urea, this pristine g-C₃N₄ exhibits a typical silk-like morphology of thin nanosheets (Fig. S2), which could facilitate a faster charge transfer and separation than that on densely stacked layers [11]. Fig. 3a shows flower-like MoS₂ nanostructure with the high-resolution TEM (HRTEM) image as shown in Fig. 3b. The constituents of the ultrathin nanosheets show crumpling and bending flakes with thickness of 5–10 nm, which

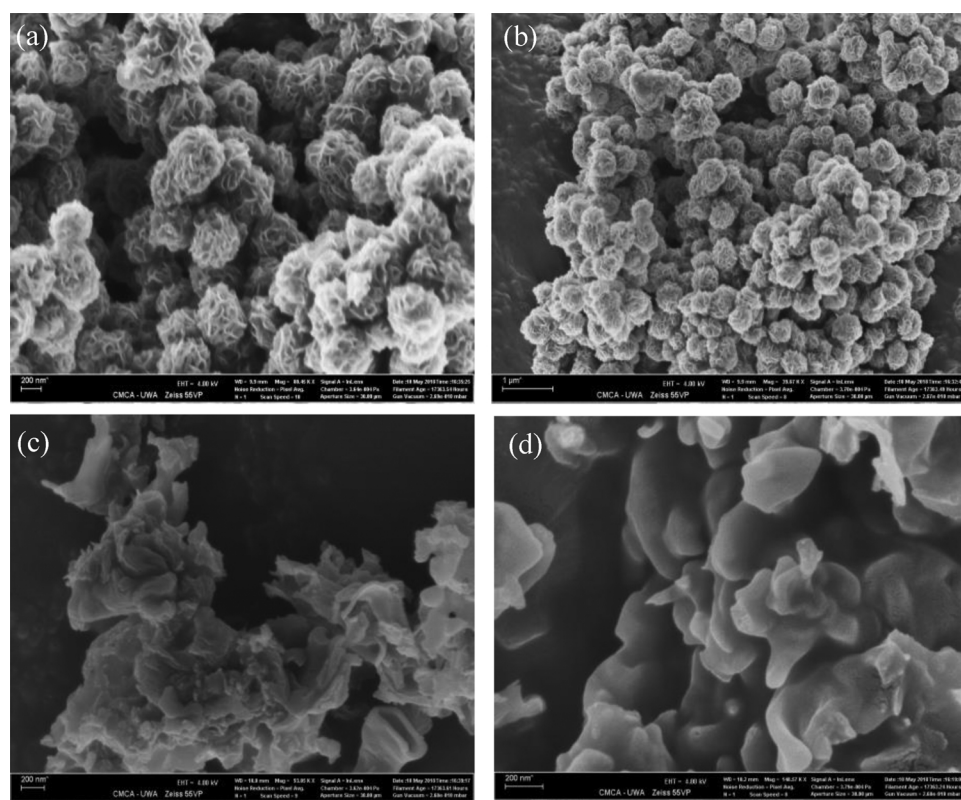


Fig. 2. SEM images of (a–b) MoS₂; (c) 0.5% MSNS-CN; (d) g-C₃N₄.

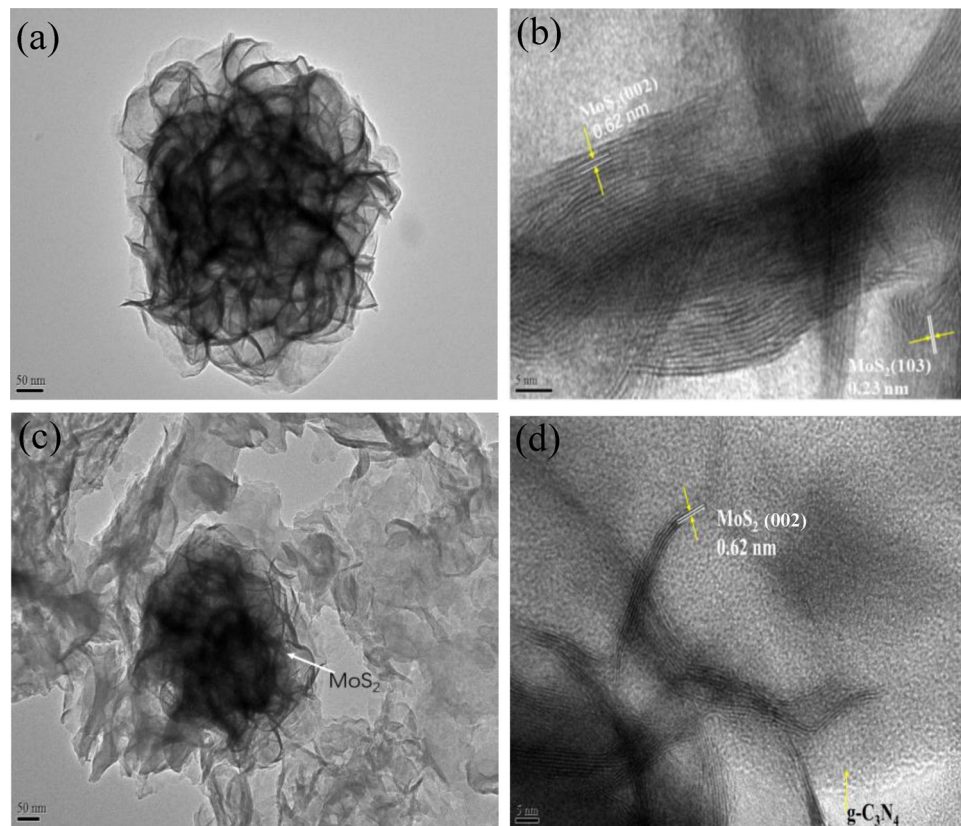


Fig. 3. TEM images of MoS₂ (a) and 0.5% MSNS-CN (c); HRTEM images of MoS₂ (b) and 0.5% MSNS-CN (d).

agrees well with the SEM observations. Ordered lattice fringe (103) together with commonly observed lattice fringe (002) can be observed clearly, showing a lattice spacing of 0.23 nm and 0.62 nm with a good crystallinity[7,48]. This is in accordance with the XRD results in Fig. 1a for MoS₂ nanostructure. The specific exposed crystal planes other than the chemically inert basal plane of (002) could benefit the exposure of more active sites for HER performance [49].

TEM and HRTEM images of 0.5% MSNS-CN sample are shown in Fig. 3c–d, revealing that the crystallized MoS₂ with thin-layers has covered the surface of g-C₃N₄ with a similar layered structure. As can be seen in Fig. 3d, approximately 5–8 slabs of MoS₂ have been uniformly deposited on g-C₃N₄, forming intimate junctions during the impregnation and calcination process. According to previous reports [48,50], the similarity of layered structures between g-C₃N₄ and MoS₂ might bring in an advantage to the junction formation, promoting the growth of MoS₂ slabs on the surface of g-C₃N₄. Most of nanosheets in the MoS₂ nanoflowers (Fig. 3d) are relatively thin (averagely 3.7 nm), even thinner than that of pure MoS₂ observed in Fig. 3b. This is probably because of the ultrasonic or calcination process during the synthesis of the composite sample [19,21]. Owing to the electron-tunneling effect, thinner layers composing the 3D nanoflowers could facilitate higher charge transport efficiency across the interface than multi-layers of MoS₂ deposited on the surface of g-C₃N₄. Thus, the MoS₂ nanostructure was proven to be closely attached to the g-C₃N₄ nanosheets via their (002) crystal planes

(interlayer spacings of 0.62 nm) with an intimate interfacial contact, which contributes to efficient hydrogen evolution by means of a shorter charge transport distance, faster separation of electron-hole pairs on thin nanosheets both internally and externally. STEM-EDX elemental mapping was also implemented to investigate the distribution patterns of elements more intuitively. EDX spectrum (Fig. 4a) and high angle annular dark field scanning TEM (HAADF-STEM) image with corresponding elemental mapping images of 0.5% MSNS-CN (Fig. 4b) confirm the existence of the four major elements (C, N, Mo and S) with uniform distribution and intimate contact. Further observation reveals that flower-like MoS₂ particles are densely deposited into the broader matrix of g-C₃N₄.

To gain detailed morphology information of the sample with Pt deposition, TEM images of g-C₃N₄ decorated with both MoS₂ and Pt nanoparticles are well illustrated in Fig. S3. Clearly, the sample exhibits well-dispersed ultrafine Pt nanoparticles of ~2.5 nm on thin g-C₃N₄ nanosheets. Observation from HRTEM reveals that photodeposition of Pt was further confirmed by the (111) crystal plane with lattice spacing of ~0.222 nm.

As shown in Fig. S4a, Raman spectra were recorded to investigate the vibrational properties of the samples. Clearly, two Raman bands at ~382 and ~412 cm⁻¹ could be observed for MoS₂ sample, corresponding to the in-plane (E_{2g}¹) and the out-of-plane (A_{1g}) mode vibrations of Mo–S bond [32], respectively. Both pure g-C₃N₄ and 2.5% MSNS-CN exhibit similar band profiles due to disordered graphitic

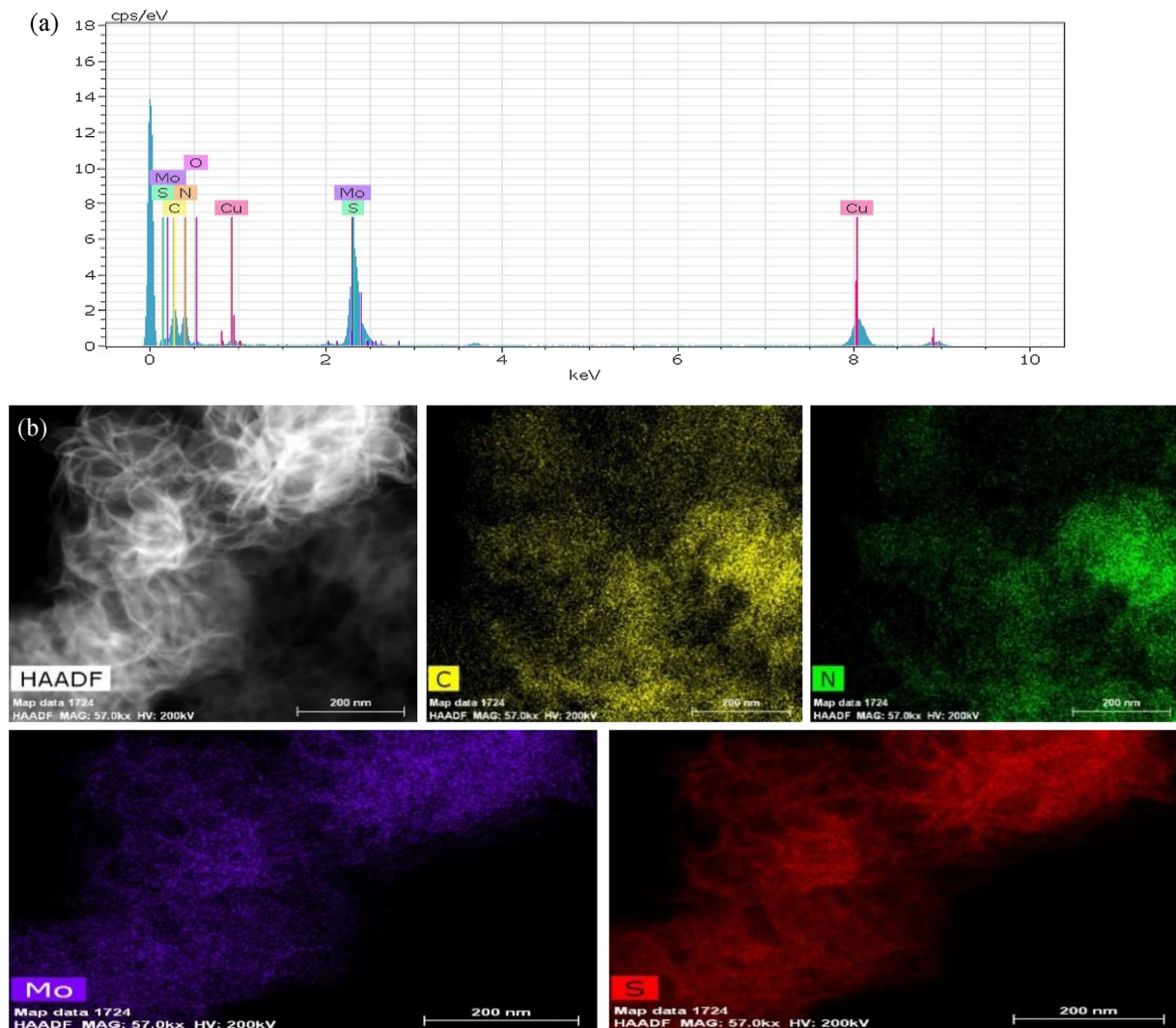


Fig. 4. (a) EDX spectrum and (b) STEM-EDX elemental mapping of the optimum 0.5% MSNS-CN composite.

carbons and other surface defects [51], except for the newly observed Raman bands at 380 cm^{-1} as a representative E_{2g}^1 mode of MoS_2 . In addition, two typical peaks at 1355 and 1570 cm^{-1} correspond to the “D” and “G” band profiles with their band intensities (I_D/I_G) increased after the modification of MoS_2 , indicating a lower graphitic carbon content in the composite sample [51]. The Raman results help convince the successful decoration of MoS_2 on the surface of $\text{g-C}_3\text{N}_4$, suggesting the intimate contact between the MoS_2 and $\text{g-C}_3\text{N}_4$.

FT-IR spectra of all the samples are illustrated in Fig. S4b, and all the MSNS-CN composite samples follow the similar chemical skeleton of pure $\text{g-C}_3\text{N}_4$ with no obvious peaks of MoS_2 detected, in good agreement with previous XRD analysis. The absorption bands dominate in the range of $1200\text{--}1700\text{ cm}^{-1}$, presenting characteristic peaks at $1228, 1329, 1427, 1567$ and 1632 cm^{-1} . These peaks can be ascribed to typical stretching modes of CN heterocyclic compounds[52]. Meanwhile the sharp peak appearing at 805 cm^{-1} represents the vibration mode of the tri-s-triazine (melem) unit. It can be seen that there is apparent decrease of peak intensity or red shift in peak location with increasing MoS_2 content. These changes might be attributed to the hydrogen bonding interactions of $\text{S}\cdots\text{H}\cdots\text{N}$ after modification with sulfur atoms of MoS_2 , helping to proving the formation of strong interfacial interactions between MoS_2 and $\text{g-C}_3\text{N}_4$ [53,54].

3.2. Optical properties

UV-vis diffuse reflectance spectra (DRS) of $\text{g-C}_3\text{N}_4$, MoS_2 and MSNS-CN composites are displayed in Fig. 5 and Fig. S5. As it is seen from Fig. 5a, the absorption edge of pure $\text{g-C}_3\text{N}_4$ is estimated to be around 479 nm and most of the composite samples show a slight red-shift to the broader range of visible light. Furthermore, the introduction of MoS_2 has enhanced the light absorption capacity both in UV and visible light range, which might contribute to the enhanced production of electron-hole pairs. Based on Tauc's equation $(\alpha h\nu)^n = k(h\nu - E_g)$ (where α , ν and E_g represent absorption factor, light frequency and band gap energy, respectively; $n = 1/2$ for indirect-gap semiconductors and $n = 2$ for direct gap semiconductors) [15,37], the band-gap energies of all the samples were calculated and listed in Table S1. The corresponding band-gap energies are displayed in Fig. 5b and Fig. S5a (inset). The shifts of the band-gap energy of the composites also prove that the MoS_2 decoration has changed the properties of $\text{g-C}_3\text{N}_4$ due to the formation of effective heterojunction. The band gap value for pure $\text{g-C}_3\text{N}_4$ was estimated to be 2.61 eV , which conforms to the previous reports [17,55,56]. MoS_2 exhibits a relatively wide absorption throughout UV-vis light region. Compared to the absorption edge of bulk MoS_2 with a narrow band gap at around 1.23 eV in previous work [57,58], an obvious blue-shift from MoS_2 thin nanosheets was noticed with a band gap value of 1.96 eV in Fig. S5 due to strong quantum confinement effects, which makes MoS_2 a possible efficient visible-light co-catalyst.

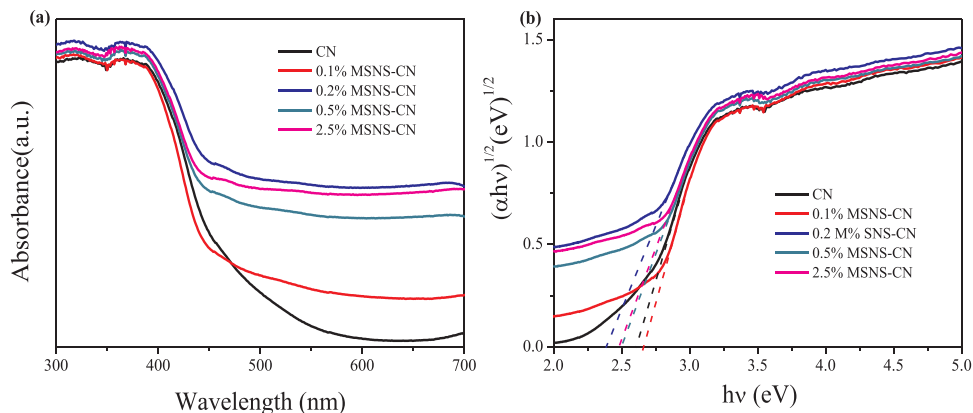


Fig. 5. (a) UV-vis DRS spectra and (b) the plots of $(\alpha h\nu)^{1/2}$ versus band-gap energy ($h\nu$) of MSNS-CN composite samples.

3.3. Photocatalytic HER activity and stability

From our previous work [27], a 0D (MoS_2)/2D ($\text{g-C}_3\text{N}_4$) heterojunction has been fabricated with an optimal photocatalytic H_2 evolution rate at $576.6\text{ }\mu\text{mol h}^{-1}\text{ g}^{-1}$. For comparison, a 2D (MoS_2)/2D ($\text{g-C}_3\text{N}_4$) heterojunction was also prepared and presented a relatively lower photocatalytic HER rate at $425.4\text{ }\mu\text{mol h}^{-1}\text{ g}^{-1}$ under the same reaction conditions. To verify if a novel 3D (MoS_2)/2D ($\text{g-C}_3\text{N}_4$) superstructure would facilitate a more superior photocatalytic H_2 evolution performance, the similar study over pure MoS_2 and MSNS-CN with different MoS_2 contents were also conducted (Fig. 6). It is worth noticing that MoS_2 alone is not active for photocatalytic H_2 evolution from water, although being an excellent co-catalyst for $\text{g-C}_3\text{N}_4$. The overall evolved hydrogen over pure $\text{g-C}_3\text{N}_4$ after 4 h was only $62.4\text{ }\mu\text{mol}$. As the MoS_2 content increases, the rate of photocatalytic H_2 evolution increases accordingly and reaches the peak value of $867.6\text{ }\mu\text{mol h}^{-1}\text{ g}^{-1}$ at 0.5% MSNS-CN, which was approximately 2.8 times higher than pristine $\text{g-C}_3\text{N}_4$. As listed in Table S2, 0.5% MSNS-CN sample in this study shows the best photocatalytic HER activity compared to previous studies, which is 1.5 times as high as that of 5% MSQD-CN [27] (the optimal one for 0D (MoS_2)/2D ($\text{g-C}_3\text{N}_4$) composites) under the same reaction system. However, the hydrogen evolution activity of MSNS-CN decreased with further increasing MoS_2 loading, probably due to the blocking effect for light absorption and the reduced active sites on the surface of $\text{g-C}_3\text{N}_4$ [14,59]. Earlier studies show that thin-layered MoS_2 nanosheets favor accelerated charge transport and separation via a shorter path, thus leading to the enhanced photocatalytic efficiency for hydrogen evolution [23,60]. As a recognized effective HER catalyst [22,61,62], MoS_2 nanosheets with thin layers and a defect-rich structure often boost a superior HER activity by strengthening the exposure of active edge planes except for preferentially exposed stable planes of the (002) [21,49], contributing to a higher performance of photocatalytic H_2 evolution. For comparison, photocatalytic H_2 evolution testing with 0.5% MSNS-CN without deposition of Pt under the same reaction conditions. As shown in Fig. S6, only $15.6\text{ }\mu\text{mol}$ of hydrogen was produced after 4 h with an average photocatalytic H_2 evolution rate of $78.0\text{ }\mu\text{mol h}^{-1}\text{ g}^{-1}$. After deposition of Pt, the H_2 evolution rate has been enhanced to $867.6\text{ }\mu\text{mol h}^{-1}\text{ g}^{-1}$. Indeed, co-catalyst Pt plays an important role in hydrogen generation process with the detailed mechanism further discussed later.

To further study the photocatalytic H_2 evolution activity of 0.5% MSNS-CN under visible light only, photocatalytic HER experiments were conducted with a light cutoff filter ($\lambda > 420\text{ nm}$). Fig. S7 illustrates that 0.5% MSNS-CN exhibits the outstanding H_2 evolution rate at $133.50\text{ }\mu\text{mol h}^{-1}\text{ g}^{-1}$, which is about 5 times as high as that of pure $\text{g-C}_3\text{N}_4$ ($26.56\text{ }\mu\text{mol h}^{-1}\text{ g}^{-1}$). The overall hydrogen evolution amounts over the 0.5% MSNS-CN and $\text{g-C}_3\text{N}_4$ reach 533.99 and $106.26\text{ }\mu\text{mol g}^{-1}$, respectively, after 4 h visible light irradiations. A full

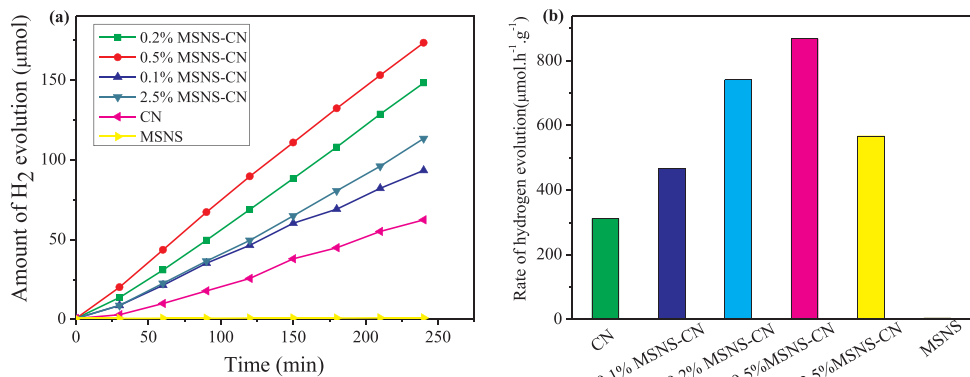


Fig. 6. Comparison of (a) photocatalytic H₂ evolution amount and (b) photocatalytic H₂ evolution rate over different samples under simulated solar light irradiations. (25 vol% methanol, 2.0 wt% Pt, 0.05 g catalyst in 120 mL aqueous solution).

comparison of photocatalytic H₂ evolution performance on 0.5% MSNS-CN sample between simulated sunlight and visible light irradiations is illustrated in Fig. 7a. Both of the hydrogen production increased continuously with the prolonged irradiation time, while the production amount of H₂ outperformed dramatically under simulated solar light than that under visible light irradiations. Concerning the overall H₂ output, the elevation efficiency of 0.5% MSNS-CN relative to pure g-C₃N₄ was even more prominent under visible light irradiations. After 4 h, the corresponding H₂ evolutions reached 3470.40 μmol g⁻¹ and 533.99 μmol g⁻¹, respectively. Thus, 0.5% MSNS-CN was proven to exhibit optimal hydrogen evolution performance and was chosen to further study the intrinsic photocatalytic mechanism. Apart from its excellent photocatalytic H₂ evolution performance, 0.5% MSNS-CN also maintains a high stability with five-cycle runs under simulated sunlight irradiations. In detail, a time-circle photocatalytic H₂ evolution test was performed with evacuation every 4 h (Fig. 7b). After a 20 h successive reaction, the photocatalytic H₂ evolution amount still achieved 158.20 μmol without a noticeable decrease. After the five runs, the catalysts were stored for 1 year and tested again, showing a similar catalytic performance with only a decay of 18%. This decrease in the photocatalytic performance could be attributed to the various degrees of break down and depletion of 3D flower-like MoS₂ compared to the pristine hybrid material, which could be further convinced by the relevant TEM and EDS tests in Fig. S8. The XRD analysis from Fig. S8b also reveals that the crystal structure and core skeleton of 0.5% MSNS-CN did not change after the long-time testing. These results well illustrated that the as-prepared 0.5% MSCN-CN composite has formed a solid heterostructure with a sound stability and durability.

3.4. Photocatalytic mechanism

To gain insight into the enhanced charge transfer and separation

efficiency of the interface between g-C₃N₄ and MoS₂ nanojunction, photoluminescence (PL), electrochemical impedance spectroscopy (EIS), transient photocurrent responses and Mott-Schottky (M-S) measurements were conducted. Fig. 8a displays the PL spectra of all the MSNS-CN samples at an excitation wavelength of 325 nm. All the samples demonstrate similar emission trends with a main emission peak centered at 460 nm, originating from the recombination of the photo-induced electrons and holes corresponding to the band gap transition [33,40]. Compared to pure g-C₃N₄, the introduction of MoS₂ leads to a much lower PL intensity, indicating the improved separation efficiency and suppressed recombination rate of the induced charge carriers at the interface. This PL result matches well with the photocatalytic H₂ evolution activities as discussed in Fig. 6.

Furthermore, the photoelectrochemical properties were studied focusing on the optimal 0.5% MSNS-CN sample to probe into the inherent mechanism for the enhancement of charge carrier separation and transportation. The photocurrent I-t curves for g-C₃N₄ and 0.5% MSNS-CN samples were acquired under intermittent simulated solar light irradiations (Fig. 8b). It can be seen that the binary photocatalyst exhibits a much higher photocurrent density with a good stability after four cycles than pure g-C₃N₄, indicating that the existence of MoS₂ is able to boost more efficient interfacial charge transfer between the g-C₃N₄ and MoS₂. As a most convincing technique in electrochemical study, EIS was employed to further confirm the interfacial charge transport resistances [63–65]. Fig. 8c shows that the arc radius for 0.5% MSNS-CN film is much smaller than that of pure g-C₃N₄, suggesting an improved charge migration efficiency across the electrode/electrolyte due to higher conductivity and lower charge transfer resistance of MoS₂. This result is in good agreement with the PL observation, confirming that the heterojunction between g-C₃N₄ and MoS₂ accelerates the electron-hole separation and transport process, and contributes to the enhancement of photocatalytic H₂-production activity.

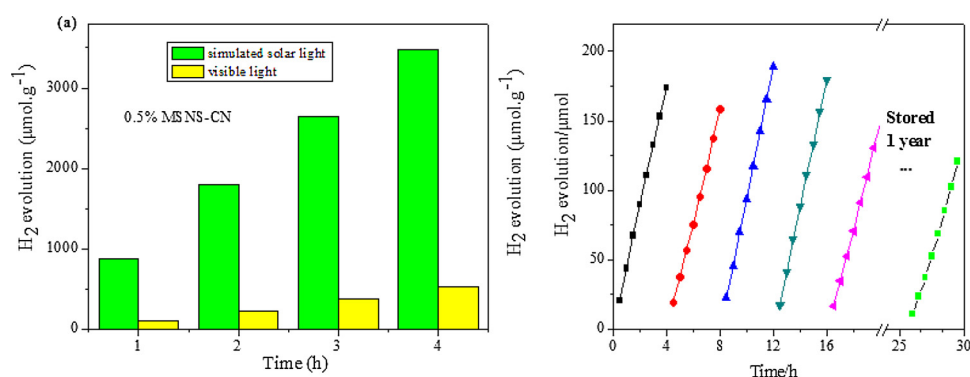


Fig. 7. (a) Rate of H₂ production over CN and 0.5% MSNS-CN with various light sources and (b) Cyclic runs for the photocatalytic H₂ production on 0.5% MSNS-CN.

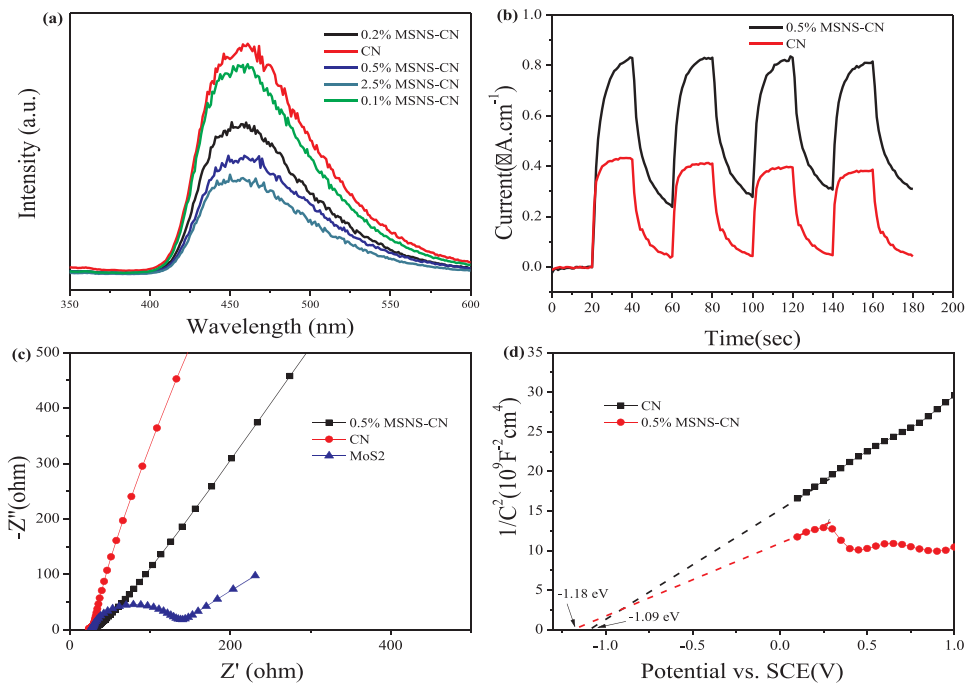


Fig. 8. (a) PL spectra of pure $\text{g-C}_3\text{N}_4$ and different MSNS-CN samples; (b) Transient photocurrent responses of $\text{g-C}_3\text{N}_4$ and 0.5% MSNS-CN; (c) Nyquist plots of electrochemical impedance spectroscopy (EIS) with different electrodes in the dark; (d) Mott-Schottky plots collected on $\text{g-C}_3\text{N}_4$ and 0.5% MSNS-CN.

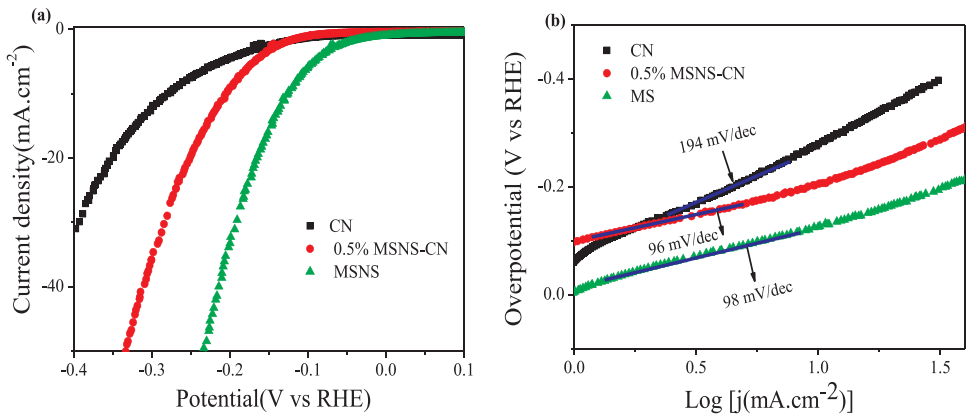


Fig. 9. (a) Polarization curves; (b) Corresponding Tafel plots of $\text{g-C}_3\text{N}_4$, MoS_2 and 0.5% MSNS-CN composite samples.

To better elucidate the intrinsic properties of the electronic band structure of the different films in contact with the electrolyte solution, the flat band potential of $\text{g-C}_3\text{N}_4$ and 0.5% MSNS-CN film electrodes were investigated using the Mott-Schottky (M-S) measurements. While plotting $1/C^2$ versus V , the flat band potentials (V_{fb}) can be acquired by extrapolating the linear part of the curves to zero [27,66,67]. Both $\text{g-C}_3\text{N}_4$ and 0.5% MSNS-CN exhibit the typical n-type semiconductor properties with the minimum potential levels of the conduction band (CB) very close to their flat band potentials. From the intercepts of the tangents on the horizontal axis in Fig. 8d, the flat band potentials of $\text{g-C}_3\text{N}_4$ and 0.5% MSNS-CN were estimated to be -1.09 V vs. SCE (-0.85 V vs. NHE) and -1.18 V vs. SCE (-0.94 V vs. NHE), respectively, displaying a slight negative shift of the conduction band potential. This upward band alignment might foster the building of an electric field at the interface between $\text{g-C}_3\text{N}_4$ and MoS_2 , which will drive the faster and more efficient separation of electrons and holes. Considering the band gap energy of 2.61 eV for $\text{g-C}_3\text{N}_4$ and 2.50 eV for 0.5% MSNS-CN accordingly, the maximum valence band (VB) energy levels were calculated to be 1.76 and 1.56 eV for $\text{g-C}_3\text{N}_4$ and 0.5% MSNS-CN, respectively. Apparently, 0.5% MSNS-CN provides a more

negative potential for photocatalytic reduction of water thermodynamically. The M-S plot collected on pure MoS_2 is displayed in Fig. S5b, in which the MoS_2 also shows a typical n-type feature [68] with a flat band potential at around -0.66 V vs. SCE (-0.42 V vs. NHE).

To further confirm the separation efficiency of the charge carriers between $\text{g-C}_3\text{N}_4$ and MoS_2 , time-resolved fluorescence emission decay spectra were recorded (Fig. S9). The curves were fitted based on equation $f(t) = A + B_1 \times \exp(-t/T_1) + B_2 \times \exp(-t/T_2)$ [69] with the parameters summarized in Table S3, where T_1/T_2 represent lifetimes, B_1/B_2 represent pre-exponential factors and T_{avg} means the average lifetime of the carriers. The average decay lifetime was increased from 3.569 to 3.881 ns after the introduction of 0.5 wt% MoS_2 . The slightly prolonged lifetime of the charge carriers gives rise to the probability of more involvement in photocatalytic reduction reaction instead of recombination, indicating a higher transfer and separation efficiency. This result well supplements the above PL and photoelectrochemical findings in elucidating the promoted photocatalytic reaction mechanism.

The electrochemical HER performance of the optimal 0.5% MSNS-CN sample was then evaluated in comparison with pure $\text{g-C}_3\text{N}_4$ and

MoS_2 to further identify the roles of MoS_2 as a co-catalyst during the photocatalytic H_2 evolution process. The linear sweep voltammetry (LSV) curves were recorded in N_2 -saturated 0.5 M H_2SO_4 solution with a three-electrode system showing their HER activity. As can be seen in Fig. 9a, all the electrodes display apparent cathodic currents within the range of 0 ~ −0.4 V (versus RHE) with increasing amount of H_2 gas bubbles from the surface of the working electrode (Fig. S10). In detail, pure MoS_2 exhibits the highest electrocatalytic activity among the three samples with the lowest onset potential at −0.01 V vs RHE, while the HER catalytic performance of pure $\text{g-C}_3\text{N}_4$ was very poor showing a high onset potential of −0.12 V vs RHE and a relatively weak cathodic current. After modification with MoS_2 , the HER activity was slightly enhanced with the onset potential shifting to −0.09 V vs RHE, and a significant current of 10 mA cm^{-2} for H_2 evolution could be obtained at an extremely low overpotential of −0.20 V vs RHE. In addition, Tafel slope is also addressed to reflect the inherent properties of the electrocatalysts, which can be inferred from the linear portions of the Tafel plots based on the Tafel equation ($\eta = b \log j + a$, where η is the overpotential; b is the Tafel slope and j represents the current density) [6,44,70]. As it is shown in Fig. 9b, the Tafel slopes for $\text{g-C}_3\text{N}_4$, MoS_2 nanosheet and 0.5% MSNS-CN were estimated to be 194, 98 and 96 mV/dec, respectively. The smaller slope of 0.5% MSNS-CN relative to $\text{g-C}_3\text{N}_4$ also signifies a much improved HER performance kinetically. Compared to pure $\text{g-C}_3\text{N}_4$, the HER performance of 0.5% MSNS-CN was enhanced with a lower onset potential, a higher current density (at a fixed voltage, for example, −0.3 V), as well as a much smaller Tafel slope, thus the activation barriers were decreased, leading to improved H_2 evolution kinetics and activity. The EIS results in Fig. 8c may well explain the enhanced HER performance of 0.5% MSNS-CN for its low charge-transfer resistance and high conductivity.

Given the discussions above, the improved photocatalytic H_2 -evolution activity of the MSNS-CN composites can be attributed to the enhanced light absorption ability, decreased electrocatalytic H_2 evolution overpotentials as well as more efficient transfer and separation of photoinduced electron/hole pairs. On one hand, the introduced MoS_2 co-catalyst can serve as an electron acceptor with a higher conductivity and lower charge-transfer resistance. Under light irradiations, the photoinduced electrons from the conduction band of $\text{g-C}_3\text{N}_4$ will be transferred to the lower conduction band of MoS_2 . The intimate interfacial contact between $\text{g-C}_3\text{N}_4$ and MoS_2 is able to foster a shorter charge transport distance and a faster transfer efficiency of electrons. Without loading of MoS_2 as the co-catalyst, the photo-generated electrons and holes will easily recombine at both bulk and surface of $\text{g-C}_3\text{N}_4$. MoS_2 would act as active sites to accelerate the overall photocatalytic and electrochemical H_2 evolution reactions. The unsaturated active S atoms along the exposed edges over the basal planes of MoS_2 layers can bond to H^+ in the solution, which will then be reduced to H_2 easily by trapping electrons [21]. On the other hand, MoS_2 could serve as an excellent co-catalyst owing to its lower electrocatalytic H_2 -evolution overpotential relative to pure $\text{g-C}_3\text{N}_4$, which also plays a key role as active sites over $\text{g-C}_3\text{N}_4$ nanosheets. The loading ratio of 0.5% with the best photocatalytic H_2 -evolution performance may reach an optimal balance between charge carriers transfer at the interface and light absorption on $\text{g-C}_3\text{N}_4$ as the light-harvesting semiconductor. Additionally, the loading of MoS_2 also increases the water reduction ability by slightly shifting the conduction band to a more negative potential position. Overall, the energy band structure and proposed mechanism for charge transfer and separation scheme are clearly illustrated in Fig. 10. It is shown in Fig. 10a that the conduction band of 0.5% MSNS-CN shifted upward slightly relative to pure $\text{g-C}_3\text{N}_4$, providing a more negative potential for photocatalytic water reduction reactions. The bottom energy level of the conduction band (CB) of 0.5% MSNS-CN is at −0.94 V (vs NHE, pH = 7), resulting in a stronger thermodynamic force for water reduction. The detailed mechanism for the transport and separation of electron-hole pairs were illustrated in Fig. 10b.

According to the energy band structure theory, under sunlight

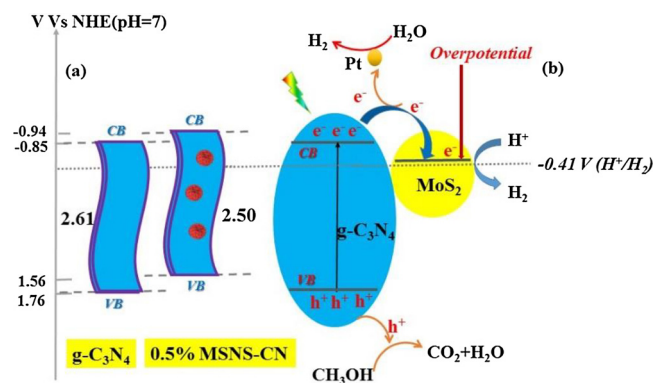


Fig. 10. (a) Energy band structure diagram of $\text{g-C}_3\text{N}_4$ and 0.5% MSNS-CN; (b) Proposed mechanism of photocatalytic H_2 evolution over $\text{g-C}_3\text{N}_4/\text{MoS}_2$ heterojunction.

irradiations, the electrons excited into the CB of $\text{g-C}_3\text{N}_4$ will be transferred to the lower CB of MoS_2 to form an electron center, while most of the holes will remain in the VB of $\text{g-C}_3\text{N}_4$ for methanol oxidation to hinder the fast recombination of electron-hole pairs. MoS_2 as a co-catalyst can act as surface active sites owing to its lower overpotential of H_2 evolution reaction and unsaturated bonds to H^+ [71]. Also because of its high electrical conductivity and low charge-transport resistance, MoS_2 stands out to be a favorable co-catalyst for electrons accepting and storing. Thus, part of the electrons will be further transferred to Pt nanoparticles to drive evolution of H_2 . Large amount of H^+ in the solution will be strongly bonded to the unsaturated active S atoms along the exposed edges over the basal planes of MoS_2 , which will then be easily reduced to H_2 by the trapped electrons in the CB of MoS_2 [59]. Under visible light irradiations, the modification of MoS_2 has promoted a wider absorption within the visible region with the band edge shifting slightly to the right. The presence of MoS_2 would decrease the reflection of light and also enhance the conductivity over $\text{g-C}_3\text{N}_4$, which accelerates the above electron transition process with strengthened photo-absorption abilities. Overall, the enhanced photocatalytic H_2 evolution performance would be attributed to the introduction of MoS_2 to form an effective interfacial contact with a decreased onset potential, lower charge-transfer resistance and higher reductive potential.

4. Conclusions

In conclusion, 3D flower-like hexagonal 2H- MoS_2 composed of nanosheets with thin-layers were prepared using a facile hydrothermal approach, and then further employed to modify $\text{g-C}_3\text{N}_4$ nanosheets with a similar layered structure to achieve $\text{MoS}_2/\text{g-C}_3\text{N}_4$ hybrid photocatalysts via a simple ultrasonic process. The as-formed intimate junctions contribute to highly enhanced photocatalytic and electrocatalytic H_2 evolution activities. The highest photocatalytic efficiency was observed on 0.5% MSNS-CN with a hydrogen evolution reaction rate of $867.6 \mu\text{mol h}^{-1} \text{g}^{-1}$ under simulated sunlight irradiations. Compared to pure $\text{g-C}_3\text{N}_4$, the photocatalytic H_2 evolution activity was elevated to about 2.8 times higher at sunlight irradiations and about 5 times higher for visible light irradiations, which could be ascribed to the flower-like MoS_2 structural features as well as the synergistic effect between the 3D MoS_2 and 2D $\text{g-C}_3\text{N}_4$. The introduction of MoS_2 nanoflowers leads to a broader absorption range and a strengthened photo-absorption capability compared to pure $\text{g-C}_3\text{N}_4$. As an electron acceptor and also the active sites over $\text{g-C}_3\text{N}_4$, the unique flower-like nanostructure of MoS_2 boosted a much higher and stable photocatalytic H_2 evolution activity with exposure of more active edge planes and shortened diffusion channels for charge transfer and separation. The proposed mechanism for the enhancement lies in the effective interfacial contact formed at the 3D (MoS_2)/2D ($\text{g-C}_3\text{N}_4$) heterojunctions with a decreased onset potential, a lower charge-transfer resistance and a higher reductive

potential with a more negative conduction band position. All the combined effects improved the photocatalytic H₂ evolution activity thermodynamically and kinetically. In addition, the lowered overpotential and smaller Tafel slope of 0.5% MSNS-CN also promise the enhanced electrocatalytic H₂ evolution performance with a decreased activation barrier and facilitated kinetics. This study provides insights into synthesizing 3D/2D hybrid photocatalysts with similar layered structures for solar hydrogen production, especially for achieving a sustainable energy solution in the future.

Acknowledgments

This work was financially supported by the Australian Research Council (DP150103026). The authors acknowledge the technical supports from the Centre for Microscopy, Characterization and Analysis, The University of Western Australia; Electron Microscope Facility, Curtin University; as well as the X-ray Surface Analysis Facility, Curtin University, funded by the Australian Research Council LIEF Grant (LE120100026).

Appendix A. Supplementary data

Supplementary material related to this article can be found, in the online version, at doi:<https://doi.org/10.1016/j.apcatb.2018.08.028>.

References

- [1] X.Y. Yu, L. Yu, H.B. Wu, X.W.D. Lou, *Angew. Chem. Int. Ed.* 127 (2015) 5421–5425.
- [2] J.A. Turner, *Science* 305 (2004) 972–974.
- [3] J. Liu, Y. Liu, N. Liu, Y. Han, X. Zhang, H. Huang, Y. Lifshitz, S.-T. Lee, J. Zhong, Z. Kang, *Science* 347 (2015) 970–974.
- [4] Y. Li, T. Takata, D. Cha, K. Takanabe, T. Minegishi, J. Kubota, K. Domen, *Adv. Mater.* 25 (2013) 125–131.
- [5] A. Kudo, Y. Misaki, *Chem. Soc. Rev.* 38 (2009) 253–278.
- [6] Y.J. Tang, Y. Wang, X.L. Wang, S.-L. Li, W. Huang, L.-Z. Dong, C.-H. Liu, Y.-F. Li, Y.-Q. Lan, *Adv. Energy Mater.* 6 (2016) 1600116.
- [7] X. Ren, L. Pang, Y. Zhang, X. Ren, H. Fan, S.F. Liu, J. Mater. Chem. A 3 (2015) 10693–10697.
- [8] A. Fujishima, *Nature* 238 (1972) 37–38.
- [9] R. Ye, H. Fang, Y.Z. Zheng, N. Li, Y. Wang, X. Tao, *ACS Appl. Mater. Interfaces* 8 (2016) 13879–13889.
- [10] J. Wen, X. Li, H. Li, S. Ma, K. He, Y. Xu, Y. Fang, W. Liu, Q. Gao, *Appl. Surf. Sci.* 358 (2015) 204–212.
- [11] G. Zhang, Z.A. Lan, L. Lin, S. Lin, X. Wang, *Chem. Sci.* 7 (2016) 3062–3066.
- [12] Y. Zhu, Q. Ling, Y. Liu, H. Wang, Y. Zhu, *Phys. Chem. Chem. Phys.* 17 (2015) 933–940.
- [13] W.-J. Ong, *Front. Mater.* 4 (2017) 11.
- [14] Y. Hou, A.B. Laursen, J. Zhang, G. Zhang, Y. Zhu, X. Wang, S. Dahl, I. Chorkendorff, *Angew. Chem. Int. Ed.* 52 (2013) 3621–3625.
- [15] H. Sun, G. Zhou, Y. Wang, A. Suvorova, S. Wang, *ACS Appl. Mater. Interfaces* 6 (2014) 16745–16754.
- [16] L. Zhou, H.Y. Zhang, H.Q. Sun, S.M. Liu, M.O. Tade, S.B. Wang, W.Q. Jin, *Catal. Sci. Technol.* 6 (2016) 7002–7023.
- [17] X. Wang, K. Maeda, A. Thomas, K. Takanabe, G. Xin, J.M. Carlsson, K. Domen, M. Antonietti, *Nat. Mater.* 8 (2009) 76–80.
- [18] L. Xu, W.-Q. Huang, L.-L. Wang, Z.-A. Tian, W. Hu, Y. Ma, X. Wang, A. Pan, G.-F. Huang, *Chem. Mater.* 27 (2015) 1612–1621.
- [19] J. Li, E. Liu, Y. Ma, X. Hu, J. Wan, L. Sun, J. Fan, *Appl. Surf. Sci.* 364 (2016) 694–702.
- [20] K. Maeda, K. Teramura, D. Lu, T. Takata, N. Saito, Y. Inoue, K. Domen, *Nature* 440 (2006) 295–295.
- [21] J. Xie, H. Zhang, S. Li, R. Wang, X. Sun, M. Zhou, J. Zhou, X.W. Lou, Y. Xie, *Adv. Mater.* 25 (2013) 5807–5813.
- [22] Y. Hou, Z. Wen, S. Cui, X. Guo, J. Chen, *Adv. Mater.* 25 (2013) 6291–6297.
- [23] Y. Yang, H. Fei, G. Ruan, C. Xiang, J.M. Tour, *Adv. Mater.* 26 (2014) 8163–8168.
- [24] Y. Yan, B. Xia, X. Ge, Z. Liu, J.Y. Wang, X. Wang, *ACS Appl. Mater. Interfaces* 5 (2013) 12794–12798.
- [25] D. Zheng, G. Zhang, Y. Hou, X. Wang, *Appl. Catal. A* 521 (2016) 2–8.
- [26] W. Fu, H. He, Z. Zhang, C. Wu, X. Wang, H. Wang, Q. Zeng, L. Sun, X. Wang, J. Zhou, Q. Fu, P. Yu, Z. Shen, C. Jin, B.I. Yakobson, Z. Liu, *Nano Energy* 27 (2016) 44–50.
- [27] Y. Liu, H. Zhang, J. Ke, J. Zhang, W. Tian, X. Xu, X. Duan, H. Sun, M.O. Tade, S. Wang, *Appl. Catal. B* 228 (2018) 64–74.
- [28] D. Lu, H. Wang, X. Zhao, K.K. Kondamareddy, J. Ding, C. Li, P. Fang, *ACS Sustain. Chem. Eng.* 5 (2017) 1436–1445.
- [29] S. Hu, W. Chen, J. Zhou, F. Yin, E. Uchaker, Q. Zhang, G. Cao, J. Mater. Chem. A 2 (2014) 7862–7872.
- [30] H. Huang, C. Du, H. Shi, X. Feng, J. Li, Y. Tan, W. Song, *Part. Part. Syst. Charact.* 32 (2015) 72–79.
- [31] W. Yu, D. Xu, T. Peng, J. Mater. Chem. A 3 (2015) 19936–19947.
- [32] F. Pan, J. Wang, Z. Yang, L. Gu, Y. Yu, *RSC Adv.* 5 (2015) 77518–77526.
- [33] J. Wen, J. Xie, Z. Yang, R. Shen, H. Li, X. Luo, X. Chen, X. Li, *ACS Sustain. Chem. Eng.* 5 (2017) 2224–2236.
- [34] J.Z. Ou, A.F. Chrimes, Y. Wang, S.-y. Tang, M.S. Strano, K. Kalantar-zadeh, *Nano Lett.* 14 (2014) 857–863.
- [35] M. Chhowalla, G.A. Amaralunga, *Nature* 407 (2000) 164–167.
- [36] Y. Liu, Y. Zhao, L. Jiao, J. Chen, J. Mater. Chem. A 2 (2014) 13109–13115.
- [37] H. Zhang, W. Tian, L. Zhou, H. Sun, M. Tade, S. Wang, *Appl. Catal. B* 223 (2017) 2–9.
- [38] S.M. Lyth, Y. Nabae, S. Moriya, S. Kuroki, M.-a. Kakimoto, J.-i. Ozaki, S. Miyata, *J. Phys. Chem. C* 113 (2009) 20148–20151.
- [39] S. Yan, Z. Li, Z. Zou, *Langmuir* 25 (2009) 10397–10401.
- [40] X. Jin, X. Fan, J. Tian, R. Cheng, M. Li, L. Zhang, *RSC Adv.* 6 (2016) 52611–52619.
- [41] A. Thomas, A. Fischer, F. Goettmann, M. Antonietti, J.-O. Müller, R. Schlögl, J.M. Carlsson, *J. Mater. Chem.* 18 (2008) 4893–4908.
- [42] V.N. Khabashesku, J.L. Zimmerman, J.L. Margrave, *Chem. Mater.* 12 (2000) 3264–3270.
- [43] L. Ge, F. Zuo, J. Liu, Q. Ma, C. Wang, D. Sun, L. Bartels, P. Feng, *J. Phys. Chem. C* 116 (2012) 13708–13714.
- [44] X. Ren, L. Pang, Y. Zhang, X. Ren, H. Fan, S. Liu, J. Mater. Chem. A 3 (2015) 10693–10697.
- [45] J. Duan, S. Chen, M. Jaroniec, S.Z. Qiao, *ACS Nano* 9 (2015) 931–940.
- [46] L. Shi, L. Liang, F. Wang, M. Liu, K. Chen, K. Sun, N. Zhang, J. Sun, *ACS Sustain. Chem. Eng.* 3 (2015) 3412–3419.
- [47] Q. Xiang, J. Yu, M. Jaroniec, *J. Am. Chem. Soc.* 134 (2012) 6575–6578.
- [48] R. Tang, R. Yin, S. Zhou, T. Ge, Z. Yuan, L. Zhang, L. Yin, *J. Mater. Chem. A* 5 (2017) 4962–4971.
- [49] X. Shang, W.-H. Hu, X. Li, B. Dong, Y.-R. Liu, G.-Q. Han, Y.-M. Chai, C.-G. Liu, *Electrochim. Acta* 224 (2017) 25–31.
- [50] Y.J. Hong, T. Fukui, *ACS Nano* 5 (2011) 7576–7584.
- [51] A.B. Jorge, D.J. Martin, M.T.S. Dhanoa, A.S. Rahman, N. Makwana, J. Tang, A. Sella, F. Corà, S. Firth, J.A. Darr, P.F. McMillan, *J. Phys. Chem. C* 117 (2013) 7178–7185.
- [52] Y. Zhang, J. Liu, G. Wu, W. Chen, *Nanoscale* 4 (2012) 5300–5303.
- [53] S.K. Kim, J.J. Wie, Q. Mahmood, H.S. Park, *Nanoscale* 6 (2014) 7430–7435.
- [54] X. Zeng, L. Niu, L. Song, X. Wang, X. Shi, J. Yan, *Metals* 5 (2015) 1829–1844.
- [55] J. Tong, L. Zhang, F. Li, M. Li, S. Cao, *Phys. Chem. Chem. Phys.* 17 (2015) 23532–23537.
- [56] P. Niu, L. Zhang, G. Liu, H.-M. Cheng, *Adv. Funct. Mater.* 22 (2012) 4763–4770.
- [57] W. Zhou, Z. Yin, Y. Du, X. Huang, Z. Zeng, Z. Fan, H. Liu, J. Wang, H. Zhang, *Small* 9 (2013) 140–147.
- [58] W. Ho, J.C. Yu, J. Lin, J. Yu, P. Li, *Langmuir* 20 (2004) 5865–5869.
- [59] H. Zhao, Y. Dong, P. Jiang, H. Miao, G. Wang, J. Zhang, *J. Mater. Chem. A* 3 (2015) 7375–7381.
- [60] X. Zong, H. Yan, G. Wu, G. Ma, F. Wen, L. Wang, C. Li, *J. Am. Chem. Soc.* 130 (2008) 7176–7177.
- [61] M.A. Lukowski, A.S. Daniel, F. Meng, A. Forticaux, L. Li, S. Jin, *J. Am. Chem. Soc.* 135 (2013) 10274–10277.
- [62] T.F. Jaramillo, K.P. Jørgensen, J. Bonde, J.H. Nielsen, S. Horch, I. Chorkendorff, *Science* 317 (2007) 100–102.
- [63] J.G. Yu, J. Jin, B. Cheng, M. Jaroniec, *J. Mater. Chem. A* 2 (2014) 3407–3416.
- [64] X.P. Xiao, J.H. Wei, Y. Yang, R. Xiong, C.X. Pan, J. Shi, *ACS Sustain. Chem. Eng.* 4 (2016) 3017–3023.
- [65] D. Jiang, J. Li, C. Xing, Z. Zhang, S. Meng, M. Chen, *ACS Appl. Mater. Interfaces* 7 (2015) 19234–19242.
- [66] J. Ke, J. Liu, H. Sun, H. Zhang, X. Duan, P. Liang, X. Li, M.O. Tade, S. Liu, S. Wang, *Appl. Catal. B* 200 (2017) 47–55.
- [67] Y. Liu, S. Ding, J. Xu, H. Zhang, S. Yang, X. Duan, H. Sun, S. Wang, *Chin. J. Catal.* 38 (2017) 1052–1062.
- [68] J. Zhang, Z. Zhu, X. Feng, *Chem. Eur. J.* 20 (2014) 10632–10635.
- [69] Y. Guo, J. Li, Z. Gao, X. Zhu, Y. Liu, Z. Wei, W. Zhao, C. Sun, *Appl. Catal. B* 192 (2016) 57–71.
- [70] X. Xu, Y. Chen, W. Zhou, Z. Zhu, C. Su, M. Liu, Z. Shao, *Adv. Mater.* 28 (2016) 6442–6448.
- [71] F. Li, J. Li, Z. Cao, X. Lin, X. Li, Y. Fang, X. An, Y. Fu, J. Jin, R. Li, *J. Mater. Chem. A* 3 (2015) 21772–21778.